Supporting Information

Seo et al. 10.1073/pnas.0907453106

SI Results

Physiological Relevance of the Nup120–Nup133 Interaction. To further characterize the physiological relevance of the Nup120–Nup133 interaction, we assessed the growth phenotype and in vivo localization of yeast strains in which the chromosomal copy of Nup120 or Nup133 was replaced by plasmid-encoded GFP fusion proteins of Nup120 or Nup133, respectively (Fig. S6). The constructs were designed based on the Nup120 structure, the Nup120–Nup133 biochemical interaction data, and the previously established mapping data of the Nup84 complex (1). For Nup120, we analyzed the full-length protein, the NTD corresponding to the crystallized fragment (residues 1–729), the CTD (residues 730–1037), and the NTD harboring the D641A mutation. For Nup133, we analyzed the full-length protein, the NTD (residues 1–520), the NTD lacking the unstructured NTE (residues 56–520), the CTD (residues 521-1157), a fragment missing the NTE (residues 56–1157), and the NTD harboring the R11A mutation (Fig. S6*A*).

The deletion of Nup120 or Nup133 resulted in a temperature-sensitive phenotype, as described previously (2). For Nup120, we found that neither the NTD nor the CTD could fully complement the Nup120 deletion phenotype. Introduction of the D641A point mutation into Nup120 or into its NTD had no significant influence on the growth rate. For Nup133, the removal of the NTD or NTE had only mild effects on cell growth, but removal of the CTD caused a strong growth phenotype. Introduction of the R11A mutation into full-length Nup133 or into the NTD caused no detectable growth retardation; however, simultaneous deletion of the CTD and NTE (Nup133 56–520) resulted in a negative growth phenotype, with significantly slower growth than even in the absence of Nup133 (Fig. S6*B*).

We then analyzed the localization of the various GFP-tagged variants of Nup120 and Nup133. The expression of GFP fusions of full-length Nup120 and Nup133 in *nup120*Δ and *nup133*Δ cells, respectively, resulted in strong nuclear rim staining, suggesting that each fusion protein can be successfully incorporated into the NPC (Fig. S6*C*). For Nup120, both the NTD and the CTD produced a similar staining, but to a lesser extent than the full-length protein, as indicated by additional cytoplasmic and nucleoplasmic staining. Moreover, the CTD resulted in an incomplete nuclear rim staining, described previously as a NPC "clustering phenotype." This phenotype was observed in knockout strains of various members of the heptameric complex (2) and has been associated with architectural defects of the NPC (3). Likewise, compared with the full-length protein, the NTD and CTD of Nup133 showed less-pronounced rim staining, with the CTD resulting in a similar NPC clustering phenotype. In contrast, the nuclear envelope localization was affected only mildly in a Nup133 fragment lacking the NTE. Strikingly, Nup133 NTD that was lacking the NTE yielded diffuse staining throughout the cell with no enrichment at the nuclear envelope.

To determine the codependence of the incorporation of Nup120 and Nup133 into the nuclear envelope, and presumably into the NPC, we created a series of yeast strains, in which the chromosomal copies of both genes were deleted and GFP-tagged variants of Nup133, together with mCherry-tagged variants of Nup120, were expressed from plasmids, according to Fig. S6*A* (Fig. S7). As expected, expression of the full-length proteins in the *nup120*Δ *nup133*Δ background restored proper nuclear envelope localization, as can be concluded from nuclear rim staining of both fusion proteins (Fig. S7*A*). In the absence of either Nup120 or Nup133, the remaining nucleoporin exhibited a clustering phenotype. Likewise, mCherry–Nup120 clustered in the absence of Nup133. We then analyzed GFP-tagged Nup133 variants (NTD, CTD, NTD ΔNTE, and NTD R11A) in the presence of mCherry-tagged Nup120 (Fig. S7*B*). None of the Nup133 variants rescued the clustering phenotype of Nup120. Although the Nup133 NTD and CTD both resulted in a similar clustering phenotype, this staining was reduced in the NTD ΔNTE and NTD R11A variants. Next, we analyzed the same Nup133 variants in the presence of mCherry-Nup120, which carries the D641A mutation. Notably, the clustering phenotype observed for the Nup133 NTD resulted in a less-pronounced clustering phenotype and more diffuse staining throughout the cell. We also analyzed mCherry-Nup120 variants (NTD, CTD, and NTD D641A) in the presence of GFP-tagged full-length Nup133 (Fig. S7*D*). In this case, Nup133 and all Nup120 variants resulted in a clustering phenotype. Strikingly, the Nup120 NTD D641A mutant yielded additional cytoplasmic staining, suggesting that it is less closely associated with the nuclear envelope. Similarly, additional cytoplasmic staining was observed for the Nup120 NTD in the presence of the Nup133 R11A mutant (Fig. S7*E*).

Finally, given the importance of the Nup120–Nup133 interaction for their nuclear envelope localization, we explored whether the disruption of this interaction alters cell growth (Fig. S6*D*). In the presence of full-length GFP-Nup133, the mCherry-tagged NTD of Nup120 partially restored cell growth at 30 °C; however, mutation of Nup133 (R11A) in combination with Nup120 NTD caused a growth reduction (Fig. S6*D*, *Top*). Cell growth was further reduced when the D641A point mutation was introduced into the Nup120 NTD (Fig. S6*D*, *Bottom*). Taken together, disruption of the Nup120–Nup133 interaction reduces cell growth, which can be explained by improper incorporation of the 2 proteins into the NPC and impaired mRNA export.

SI Materials and Methods

Plasmid Constructs. DNA fragments of *S. cerevisiae* Nup120 and of *S. cerevisiae* Nup133 were amplified by PCR from genomic DNA and cloned into a modified pGEX-4T1 (4), pGEX-6P1, a modified pET21d, and a modified pET28a vector (5). The resulting Nup120 and Nup133 fusion proteins contained a TEV- or PreScission-cleavable N-terminal GST or N-terminal PreScission-cleavable hexa-histidine tag. The Nup120 and Nup133 point mutants were generated by QuikChange mutagenesis (Stratagene) and confirmed by DNA sequencing. For the yeast experiments, various Nup120 and Nup133 fragments were subcloned into a modified pRS315 vector (6). Details of the bacterial and yeast expression constructs are given in Table S3.

Protein Expression and Purification. Nup120 and Nup133 GST fusion proteins were expressed in *E. coli* BL21-CodonPlus(DE3)-RIL cells (Stratagene). Protein expression was induced at OD_{600} of 0.7 with 0.5 mM isopropyl-β-D-thio-galactoside at 17 °C for 12–16 h in LB media containing 50 mg/L of ampicillin and 34 mg/L of chloramphenicol. The cells were lysed with a cell disrupter (Avestin) in a buffer containing 20 mM Hepes (pH 7.5), 1 M NaCl, 1 mM EDTA, and 3 mM DTT. After centrifugation at 30,000 × *g* for 30 min, the cleared lysate was applied to a GSTrap column (GE Healthcare). The column was washed with 20 mM Hepes (pH 7.5), 1 M NaCl, and 1 mM DTT, then with storage buffer [20 mM Hepes (pH 7.5), 200 mM NaCl, 1 mM DTT], and finally eluted with the storage buffer complemented with 10 mM glutathione. Following GST tag removal by TEV cleavage for 12 h at 4 °C, the

protein was applied to a HiTrapQ column (GE Healthcare) and eluted via a NaCl gradient. Fractions containing the protein were combined, concentrated, and purified over a Superdex 200 16/60 gel filtration column (GE Healthcare) in the storage buffer. Purified protein was concentrated to 30 mg/mL, flash-frozen in liquid nitrogen, and stored at -80 °C. Seleno-L-methionine labeling was performed as described previously (7), and the seleno-L-methionine protein was purified as described above.

Protein expression of the hexa-histidine–tagged Nup133 proteins and mutants was carried out in LB medium containing 50 mg/L of kanamycin and 34 mg/L of chloramphenicol and induced at OD_{600} of 0.7 by the addition of 0.5 mM isopropyl-β-D-thiogalactoside at 17 °C for 15 h. Cells were harvested by centrifugation and resuspended in a buffer containing 20 mM Tris (pH 8.0), 500 mM NaCl, 5 mM β-mercaptoethanol, 2 mM PMSF, 20 μg/mL bovine lung aprotinin, and protease inhibitor mixture (Roche). The cells were lysed with a cell disrupter (Avestin), and the lysate was centrifuged for 90 min at 40,000 $\times$ g. The lysate was then applied to a Ni-NTA column (Qiagen) and eluted via an imidazole gradient. Fractions containing Nup133 protein were pooled, dialyzed against a buffer containing 20 mM Tris (pH 8.0), 100 mM NaCl, and 5 mM DTT, and cleaved with PreScission protease (GE Healthcare) for 12 h. The protein was further purified over a MonoQ 5/50 column (GE Healthcare) and eluted via a NaCl gradient. Fractions containing the protein were pooled, concentrated, and finally purified over a Superdex 200 16/60 column (GE Healthcare). Fractions containing Nup133 protein were pooled and concentrated to 20 mg/mL for interaction experiments.

The various Nup133 NTE peptide fragments were expressed as N-terminal GST fusions with a C-terminal hexa-histidine tag. These proteins were purified using consecutive GSTrap and Ni-NTA affinity steps, as described above.

Crystallization and Structure Determination. Crystals of wild-type Nup120 were grown at 20 °C in sitting drops containing 1 μL of protein (at 6 mg/mL) and 1 μL of a reservoir solution consisting of 17% PEG 2000 MME, 0.1 M sodium citrate (tribasic dihydrate), and 0.06 M potassium thiocyanate. Introduction of the S207C mutation altered the unit cell dimensions and substantially improved the diffraction quality of the crystals, which were obtained in 0.1 M succinic acid (pH 7.0), 9%–11% (wt/vol) PEG 3350, 0.05 M sodium bromide, 9% (vol/vol) ethylene glycol, and 2.5 mM ethyl-mercuric-thio-salicylic acid (Hampton Research). Crystals of both proteins grew in the triclinic space group P1 with 4 molecules in the asymmetric unit. For cryoprotection, crystals were stabilized with 20% (vol/vol) glycerol and flash-frozen in liquid nitrogen. X-ray diffraction data were collected at the National Synchrotron Light Source (NSLS); Brookhaven National Laboratory (BNL), beamline X29; and GM/CA-CAT, Advanced Photon Source (APS), beamline 23ID-B. The X-ray diffraction data were processed using the HKL2000 denzo/scalepack package (8). The CCP4 program package (9) was used for subsequent calculations.

A SAD x-ray diffraction data set of an ethyl-mercuric-thio-salicylic acid–labeled crystal of the Ser207Cys mutant was used to identify the positions of 5 mercury atoms using SHELXD (10). Phases were calculated to 2.6 Å in SHARP (11), followed by density modification in DM (9) with solvent flattening and histogram matching. This procedure yielded an electron density map of high quality. Model building was carried out using the O (12) and COOT (13) programs. The unambiguous assignment of the protein sequence was achieved with the help of the mercury and selenium positions. The model was refined using CNS (14). No electron density was observed for residues 30–52. Residues 306–310 were not visible in the mutant structure. These residues are presumed to be disordered and thus were omitted from the final model. The stereochemical quality of the final model was assessed with PROCHECK (15) and MOLPROBITY (16). There were no residues in the disallowed region of the Ramachandran plot. Details of the data collection, phasing, and refinement statistics are provided in Table S1.

Gel Filtration Analysis. Protein interaction experiments were carried out on a Superdex 200 10/300 GL gel filtration column (GE Healthcare) equilibrated in a buffer containing 20 mM Hepes (pH 7.5), 100 mM NaCl, and 1 mM DTT. Complexes were formed by incubating approximately equimolar ratios of the various purified proteins, their mutants, or variants for 30 min on ice. Complex formation was monitored by injection of the preincubated proteins and the recombinant purified proteins in isolation. All proteins were analyzed under the same buffer conditions, and complex formation was confirmed by SDS-PAGE of the eluted fractions, followed by Coomassie brilliant blue staining.

Circular Dichroism Spectroscopy. The CD spectrum of Nup133 NTE was recorded at room temperature (≈25 °C) in an OLIS RSM 1000 circular dichroism spectropolarimeter in a fixed-slit configuration. The protein was concentrated to 0.046 mg/mL and dissolved in a 0.01 M sodium phosphate buffer and 0.05 M sodium chloride at pH 7.4. Then 200 μL of sample was loaded into a 0.1-cm path length cuvette and scanned from 250 nm to 190 nm with a 1-nm step and 1-nm bandwidth. The temperature was kept constant with a circulating water bath. Raw ellipticity values in millidegrees from the OLIS CD software were converted to molar residue ellipticity (MRE) values [Θ] using the following equation:

$$\text{MRE } [\Theta] = \text{millidegrees}/(\#\ \textit{residues} \times \textit{concentration}\ (M) \times \textit{path length}\ (cm) \times 10).$$

Analytical Ultracentrifugation. Sedimentation velocity experiments were performed at 4 °C in a Beckman Optima XL-I analytical ultracentrifuge at a rotor speed of 50,000 rpm. Double-sector cells were loaded with 400 μL of the protein sample [1.1 mg/mL of Nup120 NTD·Nup133 NTD in a solution containing 0.020 M Hepes (pH 7.4), 0.15 M NaCl, 1 mM Tris(2-carboxyethyl)phosphine (TCEP), and 410 μL of the reference solution, respectively]. The reference solution was 0.02 M Hepes (pH 7.4), 0.15 M NaCl, and 1 mM TCEP. Data were recorded with absorbance detection at a wavelength of 280 nm. The partial specific volume and the solvent density were calculated using the SEDNTERP program. The SEDFIT analysis program was used to analyze the absorbance profiles and to calculate the sedimentation coefficient distribution, c(s), which was then transformed into a molar mass distribution, c(M) (17).

ITC. ITC measurements were performed at 25 °C using a MicroCal VP-ITC calorimeter. Protein and peptide samples were extensively dialyzed against the reaction buffer [20 mM Hepes, 150 mM NaCl (pH 7.4), 1 mM TCEP] and thoroughly degassed. Then 5–10 μL of 300 μM Nup133 NTD (residues 1–487) or 450 μM Nup133 peptide (residues 1–15) were injected into 1.5 mL of 30 μM Nup120 NTD every 120 s. The heat generated from dilution was subtracted for baseline correction. Baseline corrected data were analyzed with MicroCal ORIGIN Version 5.0 software. All experiments were performed at least twice.

Yeast Strains. GFP-Nup120 and GFP-Nup133 constructs, as well as the vector control, were transformed into BY4741 *nup120*Δ::kan and *nup133*Δ::kan strains (Open Biosystems), respectively. Strains carrying Nup120 and Nup133 plasmids in a double-deletion background were generated as follows. The

Nup133 deletion was introduced into BY4741 *nup120*Δ::kanMX4 (Open Biosystems) covered by pRS416-GFP-Nup120, resulting in the strain *nup120*Δ*nup133*Δ (*MAT*a *his3*Δ*1 leu2*Δ*0 ura3*Δ*0 nup120*Δ::kanMX4 *nup133*Δ::met15 pRS416-GFP-Nup120). This strain was transformed with the plasmids pRS315-GFP-Nup133 (or mutants thereof) and pRS416-mCherry-Nup120 (or mutants thereof), as well as the respective vector controls. Transformants were selected on SD-Met-Leu-His plates and then passaged on SD-Met-Leu-His plates containing 5-fluoroorotic acid (Zymo Research). Survivors of 2 rounds of 5-fluoroorotic acid selection were confirmed for the absence of pRS416-GFP-Nup120 by their inability to grow on Ura-deficient growth medium.

FISH Growth Assay. Liquid cultures of single-deletion yeast strains carrying GFP-fusion proteins of either Nup120 or Nup133, were grown overnight at 30 °C in SD-Leu media to an OD_{600} of 0.6–0.8 before being fixed in formaldehyde. These cells were then analyzed by FISH using an Alexa-647–labeled 50-mer oligo dT probe (18). The statistical analysis was carried out using 3 independent images with 150 cells each. For the growth assay, liquid cultures of the transformants were grown overnight at 30 °C in SD-LEU media. Cells were counted and diluted to 10 million cells/mL. This stock was used to generate a 10-fold dilution series, of which 10 μL was spotted on SD-LEU plates and grown at 23 °C, 30 °C, and 37 °C for 2–3 days.

In Vivo Localization. The yeast strains were grown in selective medium, and the live cells were analyzed by fluorescence microscopy according to standard procedures, using a Carl Zeiss AxioImagerZ.1 equipped with an AxioCamMRm camera.

Illustrations and Figures. Figures were generated using PyMOL (www.pymol.org). The molecular surfaces were calculated using MSMS (19), and the electrostatic potential was calculated using APBS (20). Sequence alignments were generated using ClustalX (21) and colored with Alscript (22).

1. Lutzmann M, Kunze R, Buerer A, Aebi U, Hurt E (2002) Modular self-assembly of a Y-shaped multiprotein complex from seven nucleoporins. *EMBO J* 21:387–397.
2. Siniossoglou S, et al. (1996) A novel complex of nucleoporins, which includes Sec13p and a Sec13p homolog, is essential for normal nuclear pores. *Cell* 84:265–275.
3. Aitchison JD, Blobel G, Rout MP (1995) Nup120p: A yeast nucleoporin required for NPC distribution and mRNA transport. *J Cell Biol* 131:1659–1675.
4. Sheffield P, Garrard S, Derewenda Z (1999) Overcoming expression and purification problems of RhoGDI using a family of ''parallel'' expression vectors. *Protein Expr Purif* 15:34–39.
5. Hoelz A, Nairn AC, Kuriyan J (2003) Crystal structure of a tetradecameric assembly of the association domain of Ca2+/calmodulin-dependent kinase II. *Mol Cell* 11:1241–1251.
6. Zhao X, Wu CY, Blobel G (2004) Mlp-dependent anchorage and stabilization of a desumoylating enzyme is required to prevent clonal lethality. *J Cell Biol* 167:605–611.
7. Doublié S (1997) Preparation of selenomethionyl proteins for phase determination. *Methods Enzymol* 276:523–530.
8. Otwinowski Z, Minor W (1997) Processing of X-ray diffraction data collected in oscillation mode. *Methods Enzymol* 276:307–326.
9. CCP4 (1994) The CCP4 suite: Programs for protein crystallography. *Acta Crystallogr D* 50:760–763.
10. Sheldrick GM (2008) A short history of SHELX. *Acta Crystallogr A* 64:112–122.
11. de La Fortelle E, Bricogne G (1997) Maximum-likelihood heavy-atom parameter refinement in the multiple isomorphous replacement and multi-wavelength anomalous diffraction methods. *Methods Enzymol* 276:472–494.
12. Jones TA, Zou JY, Cowan SW, Kjeldgaard M (1991) Improved methods for building protein models in electron density maps and the location of errors in these models. *Acta Crystallogr A* 47:110–119.
13. Emsley P, Cowtan K (2004) Coot: Model-building tools for molecular graphics. *Acta Crystallogr D* 60:2126–2132.
14. Brünger AT, et al. (1998) Crystallography & NMR system: A new software suite for macromolecular structure determination. *Acta Crystallogr D* 54:905–921.
15. Laskowski RA, MacArthur MW, Moss DS, Thornton JM (1993) PROCHECK: A program to check the stereochemical quality of protein structures. *J Appl Crystallogr* 26:283–291.
16. Davis IW, et al. (2007) MolProbity: All-atom contacts and structure validation for proteins and nucleic acids. *Nucleic Acids Res* 35:W375–383.
17. Schuck P (2000) Size-distribution analysis of macromolecules by sedimentation velocity ultracentrifugation and lamm equation modeling. *Biophys J* 78:1606–1619.
18. Gwizdek C, et al. (2006) Ubiquitin-associated domain of Mex67 synchronizes recruitment of the mRNA export machinery with transcription. *Proc Natl Acad Sci USA* 103:16376–16381.
19. Sanner MF, Spehner JC, Olson AJ (1996) Reduced surface: An efficient way to compute molecular surfaces. *Biopolymers* 38:305–320.
20. Baker NA, Sept D, Joseph S, Holst MJ, McCammon JA (2001) Electrostatics of nanosystems: Application to microtubules and the ribosome. *Proc Natl Acad Sci USA* 98:10037–10041.
21. Jeanmougin F, Thompson JD, Gouy M, Higgins DG, Gibson TJ (1998) Multiple sequence alignment with Clustal X. *Trends Biochem Sci* 23:403–405.
22. Barton GJ (1993) ALSCRIPT: A tool to format multiple sequence alignments. *Protein Eng* 6:37–40.
23. Chen Y-H, Yang JT, Martinez HM (1972) Determination of the secondary structure of proteins by circular dichroism and optical rotatory dispersion. *Biochemistry* 11:4120–4131.

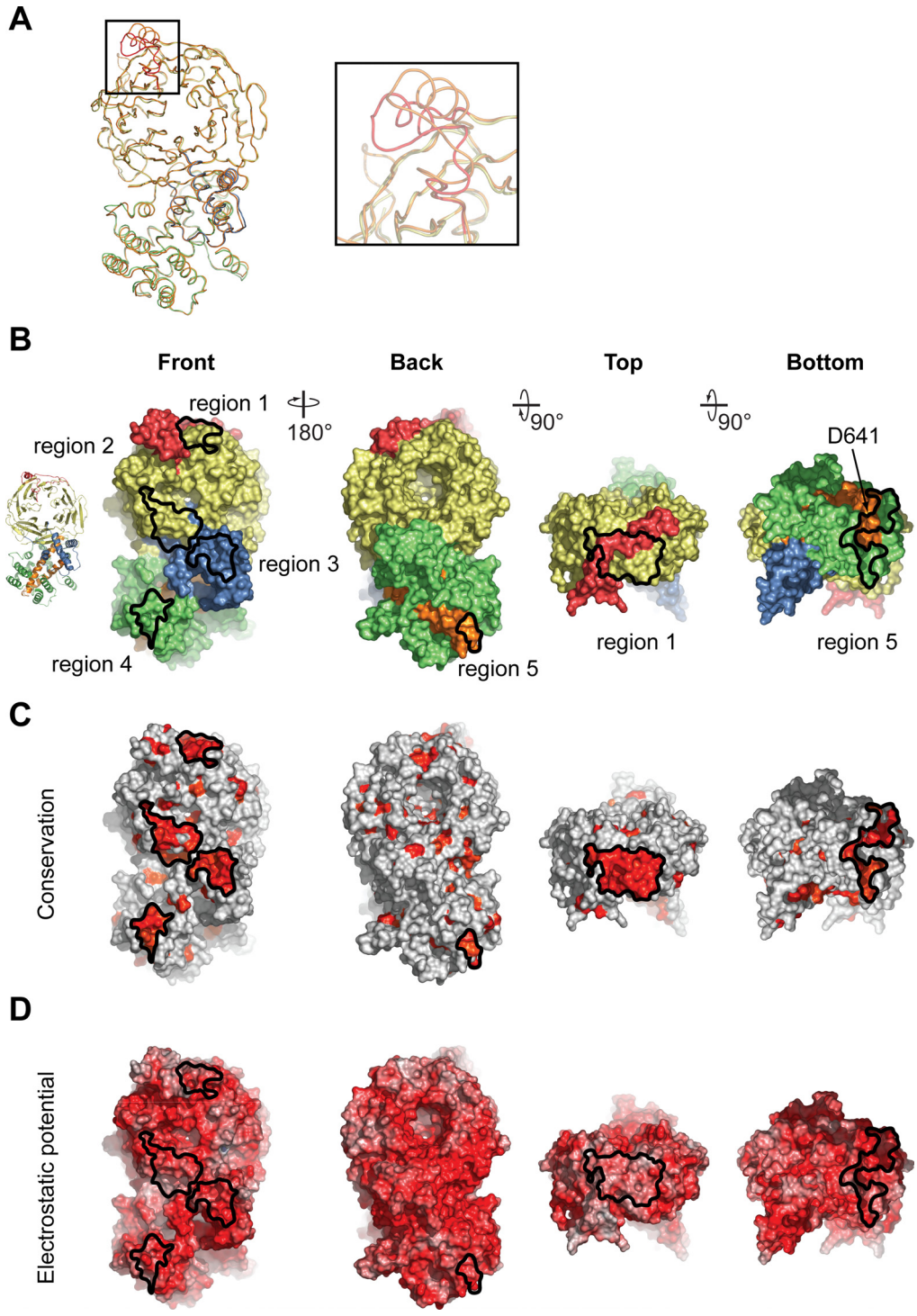

Fig. S1. Structural properties of the Nup120 NTD. (*A*) Comparison of the Nup120 structures from the wild-type and S207C mutant proteins. Coil representations of the superposition of the S207C mutant Nup120 (colored according to Fig. 1) and the wild-type Nup120 structure (orange). The inset highlights significant structural changes in the 3D4A loop. (*B–D*) Surface properties of the Nup120 NTD. (*B*) Surface representation colored according to the participation of the various domains as in Fig. 1*B*. The two left panels show the front and back views of the structure; the two right panels show the views from the top and bottom. (*C*) Surface representation colored according to a multispecies sequence alignment (Fig. S2). The conservation at each position is mapped onto the surface and is shaded in a color gradient from light yellow (40% similarity) to dark red (100% identity). (*D*) Surface representation colored according to the electrostatic potential. The electrostatic potential is plotted onto the surface and colored in a gradient from red ($-10\ k_BT/e$) to blue ($+10\ k_BT/e$). The orientation of all surface representations is identical in each column. As a reference, black lines encircle the 5 conserved surface patches.

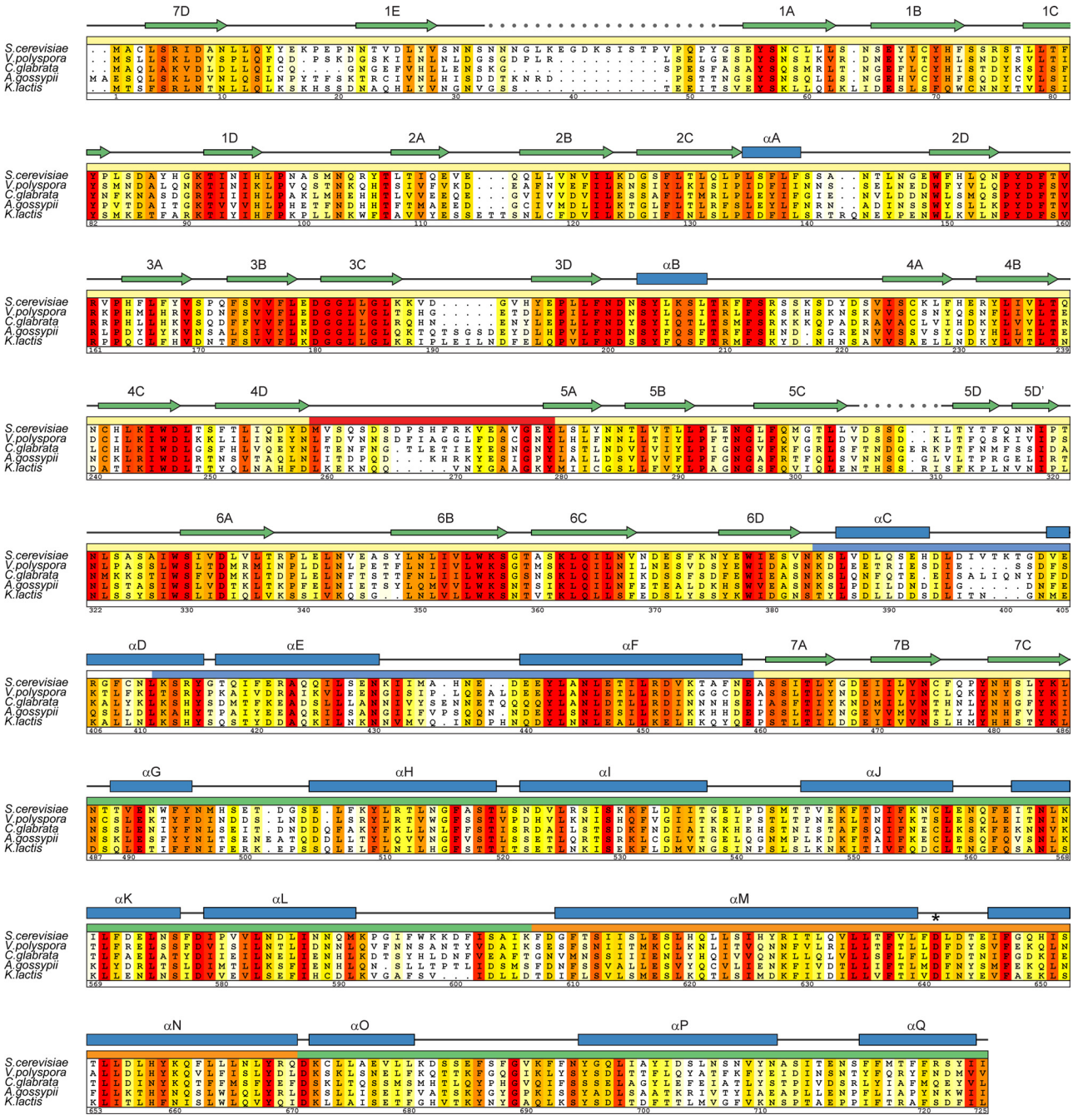

Fig. S2. Multispecies sequence alignment of Nup120 homologs. The numbering below the alignment is relative to *S. cerevisiae* Nup120. The overall sequence conservation at each position is shaded in a color gradient from yellow (40% similarity) to dark red (100% identity) using the Blosum62 weighting algorithm. The secondary structure is indicated above the sequence as blue boxes (α helices), green arrows (strands), gray lines (coil regions), and gray dots (disordered residues). The position of the invariant Asp-641 that is critical for the interaction with Nup133 is indicated by an asterisk.

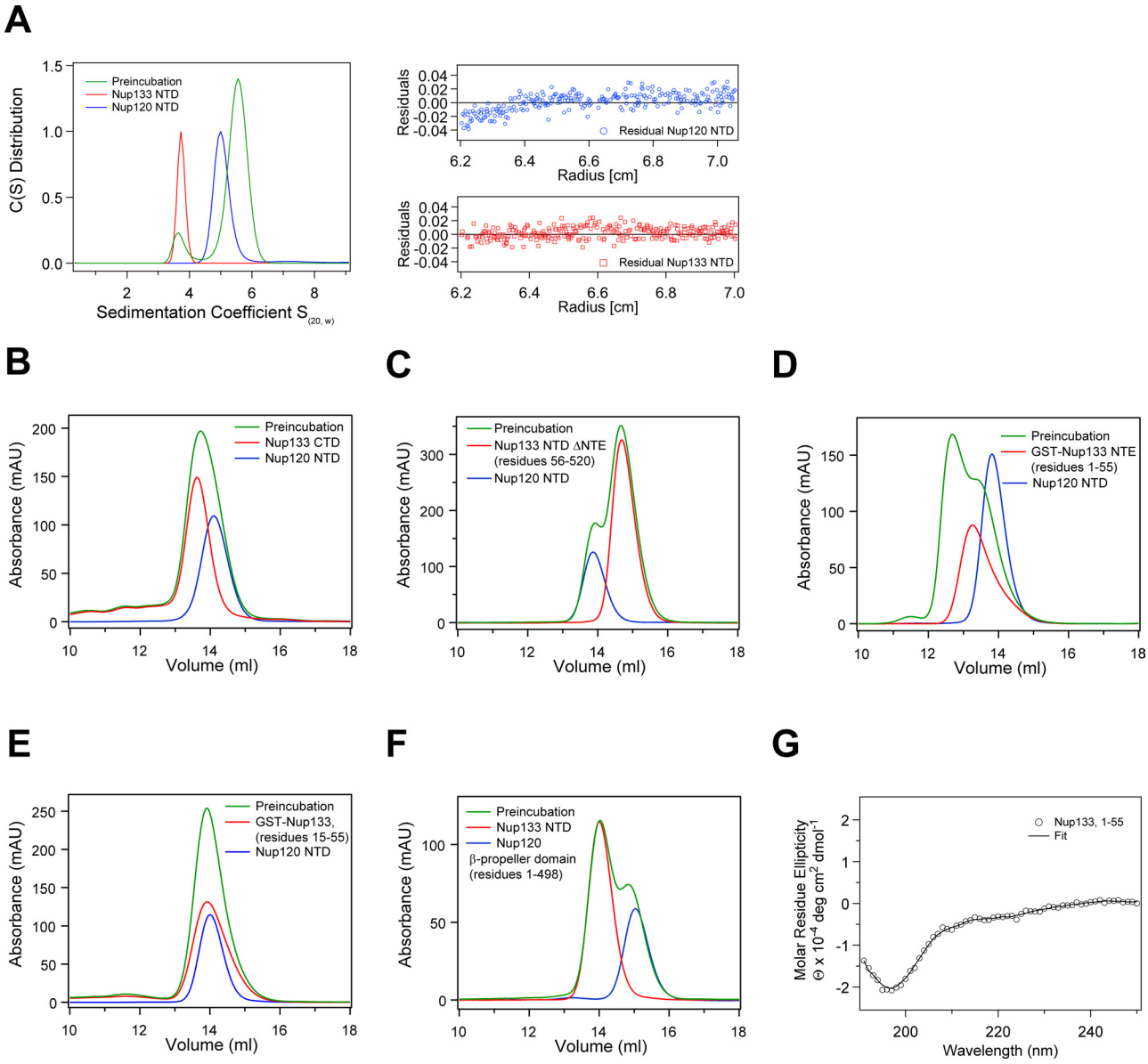

Fig. S3. Biochemical and biophysical analyses of the interaction between Nup120 and Nup133. (*A*) Sedimentation velocity analysis of the Nup120 NTD–Nup133 NTD interaction. Sedimentation coefficient distributions of the Nup120 NTD (blue), of the Nup133 NTD (red), and the Nup120·Nup133 complex (green). The large green peak indicates complex formation, while the small green peak corresponds to excess unbound Nup133 NTD. The molecular masses for Nup120 and Nup133 have been determined to 82 ± 8 (calculated 84.2 kDa) and 54 ± 2 kDa (55.7 kDa), respectively, corresponding to monomers in solution. The precise determination of the molecular mass of the Nup120·Nup133 complex is not possible, due to the presence of a second peak. (*B*–*F*) Further biochemical analysis of the Nup120–Nup133 interaction by size-exclusion chromatography. (*B*) The Nup133 CTD (residues 520–1157) and (*C*) the Nup133 NTD ΔNTE (residues 56–520), form no detectable complex with the Nup120 NTD. (*D*) The Nup133 NTE, residues 1–55, fused to GST forms a complex with Nup120 NTD. (*E*) The GST-tagged Nup133 fragment comprising residues 15–55 fails to interact with Nup120 NTD. (*F*) The Nup120 propeller domain, residues 1–498, is incapable of forming a complex with the Nup133 NTD. Gel filtration profiles of Nup120 fragments (blue), Nup133 fragments (red), and the elution profiles resulting from incubation of the 2 proteins before injection (green) are indicated. Proteins were injected at comparable concentrations. (*G*) The CD spectrum of the Nup133 NTE, residues 1–55, reveals a random coil conformation for this region (23).

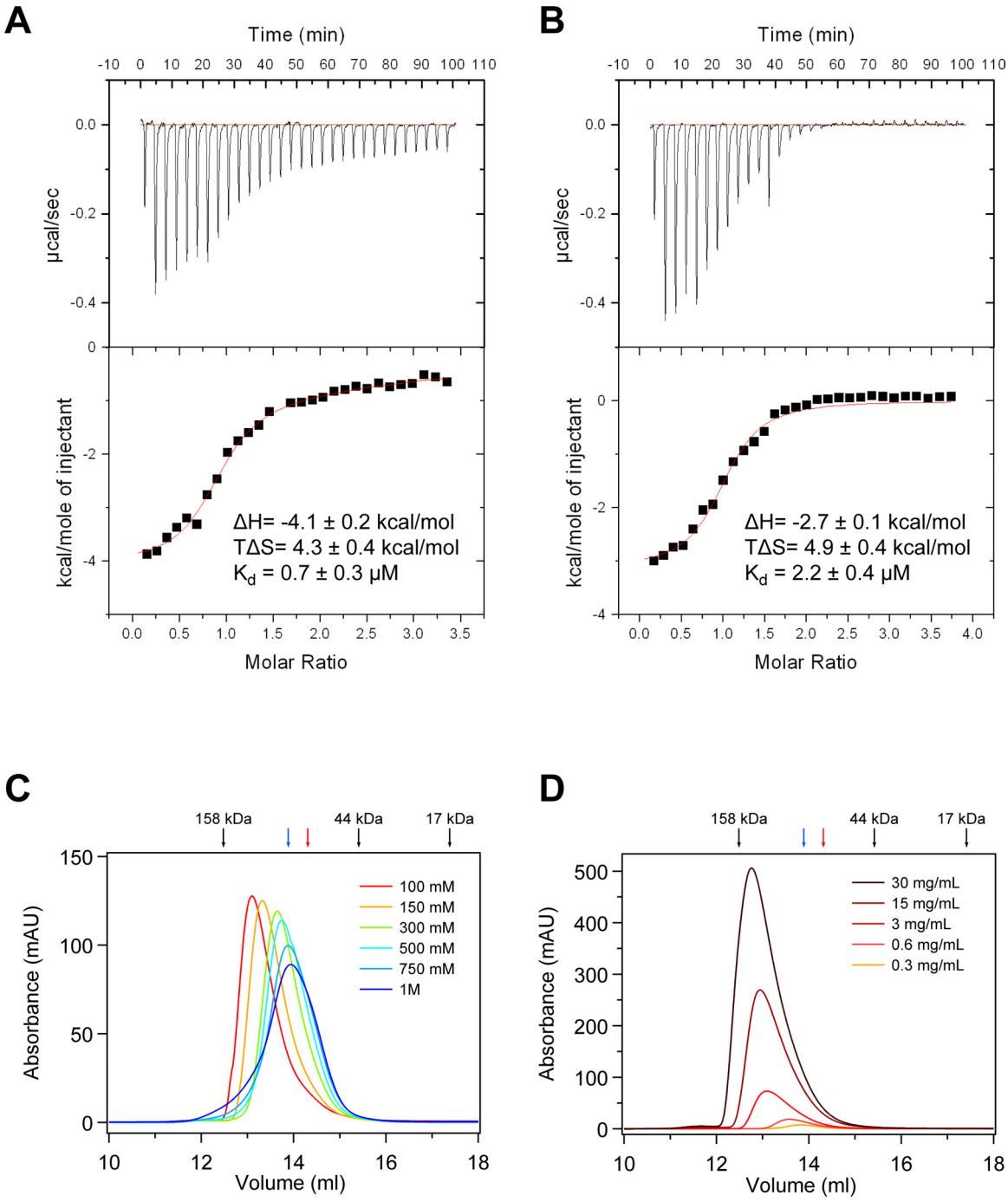

Fig. S4. Biochemical characterization of the Nup120–Nup133 interaction. (*A* and *B*) ITC analysis of the Nup120·Nup133 complex. The Nup120 NTD was titrated against (*A*) the Nup133 NTD and (*B*) a Nup133 peptide comprising residues 1–15. The dissociation constant (K_d), the binding enthalpy (ΔH), and the entropy ($T\Delta S$) were derived by curve fitting using the single-site model. The binding constant of the Nup133 peptide is decreased only slightly with respect to the entire Nup133 NTD, suggesting that the major Nup120 binding site comprises the first 15 residues of Nup133. (*C*) Salt dependence of the Nup120 NTD–Nup133 NTD interaction. Gel filtration profiles of the Nup120 NTD·Nup133 NTD complex (5 mg/mL) at various salt concentrations. The Nup120 NTD·Nup133 NTD complex eluted with an apparent molecular mass of ≈120 kDa (calculated molecular mass of the complex, ≈140 kDa) in a buffer containing 100 mM NaCl. The apparent molecular mass of the peak decreased to ≈80 kDa when examined in a buffer containing 1 M NaCl. (*D*) Concentration dependence of the Nup120 NTD–Nup133 NTD interaction. Proteins were injected at the indicated concentrations. Whereas the complex eluted with an apparent molecular mass of ≈135 kDa at 30 mg/mL, the apparent molecular mass of the peak decreased to ≈80 kDa when examined at 0.3 mg/mL. As a reference, the elution positions of molecular weight standards, Nup120 NTD (blue), and Nup133 NTD (red) are indicated. The Nup120·Nup133 complex is dynamic and governed by electrostatic interactions.

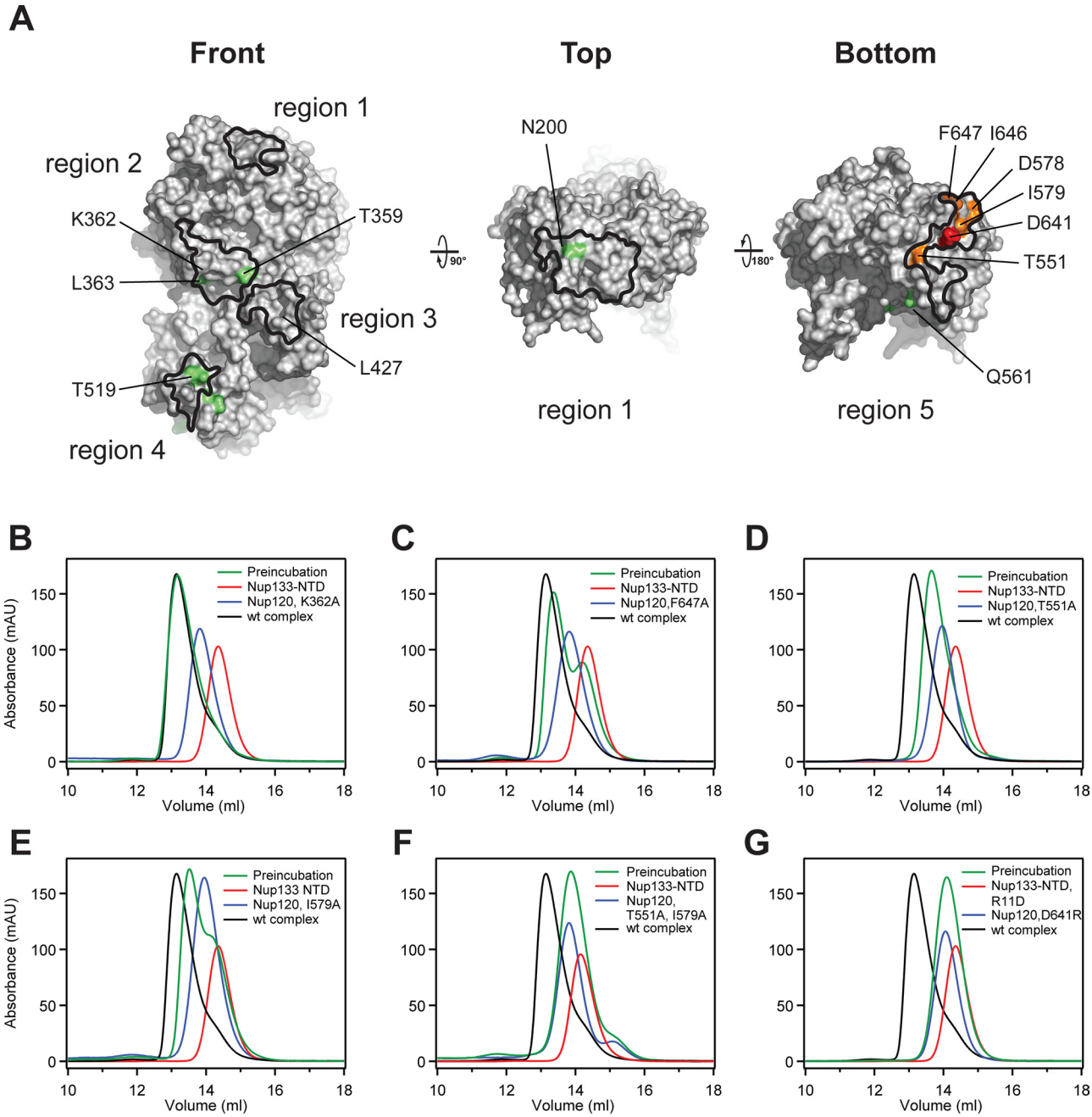

Fig. S5. Alanine scanning mutagenesis of the Nup120–Nup133 interaction. (*A*) Surface representation of the Nup120 NTD with the highlighted 5 regions identified by surface conservation analysis (Fig. S1*C*). Nup120 residues of the 5 surface patches that have no detectable effect (green), have only a moderate effect (orange), and are crucial (red) for complex formation with Nup133, as judged by size-exclusion chromatography, are indicated and mapped to the surface. (*B*–*G*) Representative gel filtration profiles for Nup120 NTD mutants that form a complex with the Nup133 NTD that is indistinguishable from the wild-type complex (*B*), have a small detectable effect (*C*), have a moderate effect (*D* and *E*), or abolish complex formation (*F* and *G*). Note that the 2 Nup120 NTD mutations in region 5, T551A and I579A, which individually have only moderate effects on complex formation, abolish complex formation when combined. Gel filtration profiles of the Nup120 NTD mutants (blue), the Nup133 NTD (red), and the elution profiles resulting from incubation of the 2 proteins before injection (green) are indicated. As a reference, the elution profile of the wild-type Nup120 NTD·Nup133 NTD complex is shown in black. Proteins were injected at comparable concentrations. The results of all analyzed mutants are presented in Table S2.

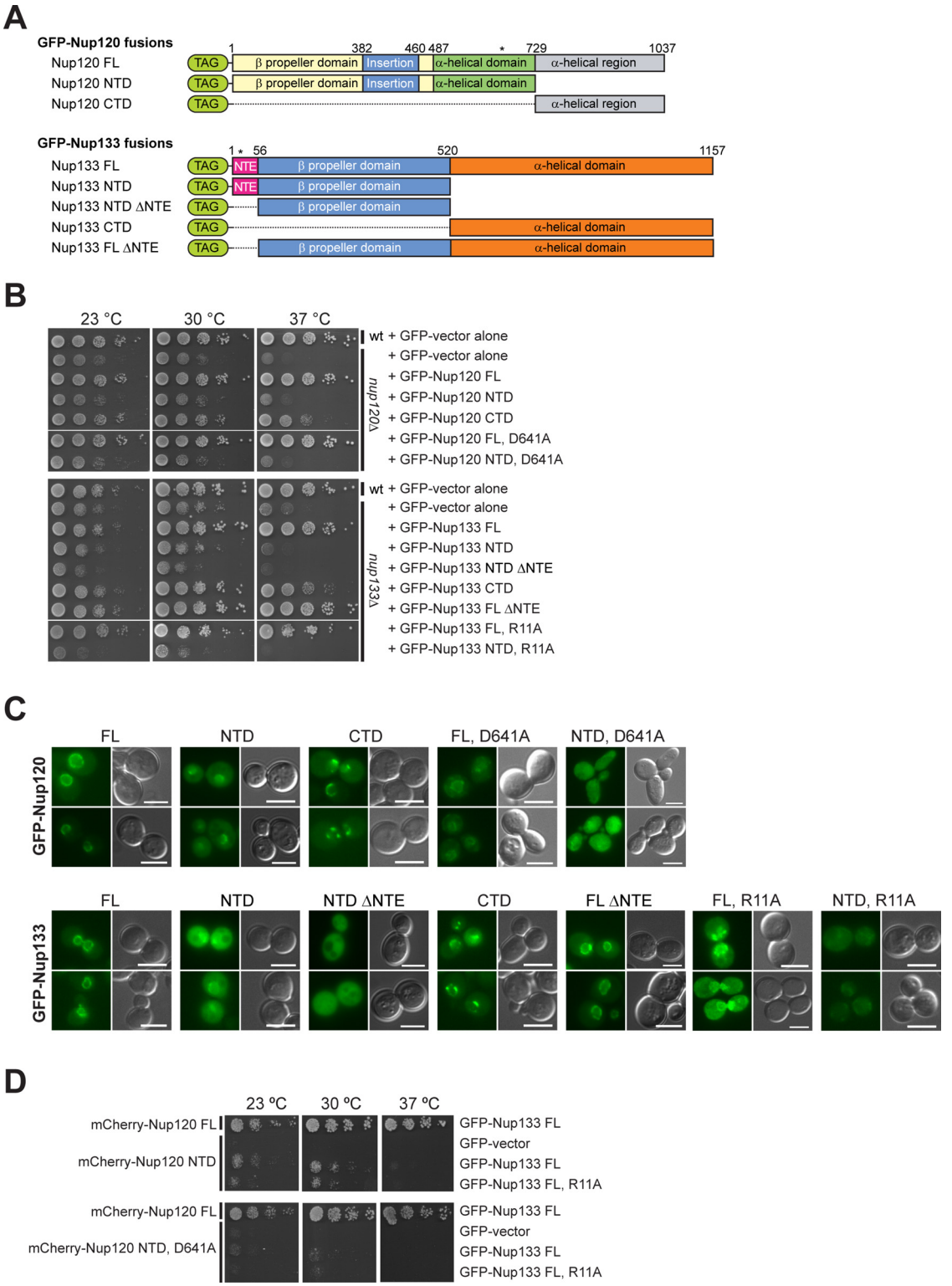

Fig. S6. Physiological relevance of the Nup120–Nup133 interaction. (*A*) The domain organization of the Nup120 and Nup133 GFP-fusion proteins is indicated. The domain organization of Nup120 is based on the structural data. For Nup133, the unstructured NTE (purple), the N-terminal β propeller domain (blue), and the C-terminal α-helical domain (orange) are indicated. (*B* and *C*) Yeast growth assay (*B*) and in vivo localization (*C*) performed using either *nup120*Δ or *nup133*Δ cells complemented with the constructs described in (*A*). (*D*) Yeast growth analysis of Nup120 and Nup133 variants in *nup120*Δ*nup133*Δ yeast cells.

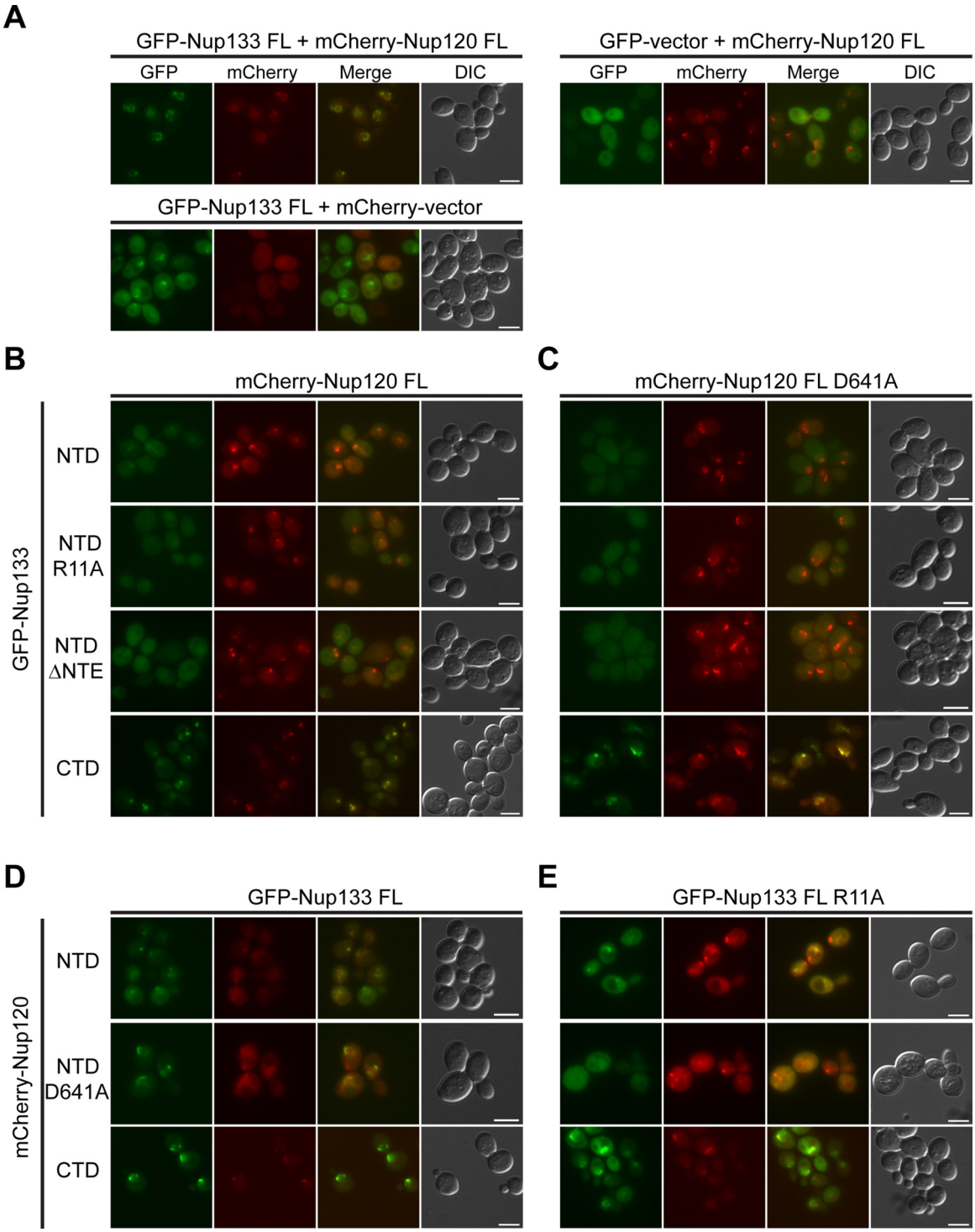

Fig. S7. Codependence of the subcellular localization of Nup120 and Nup133. Fluorescence microscopy analysis of *nup120Δnup133Δ* yeast cells complemented with various GFP-Nup133 and mCherry-Nup120 variants according to Fig. S6*A*. (*A*) While coexpression of fluorescence-tagged full-length Nup120 and Nup133 proteins results in a wild-type-like continuous rim staining, deletion of either of the 2 proteins leads to a punctate rim staining. (B–E) Analysis of *nup120Δnup133Δ* yeast cells complemented with full-length mCherry-Nup120 and various GFP-Nup133 variants (*B*), full-length mCherry-Nup120 carrying the D641A mutation and various GFP-Nup133 variants (*C*), full-length GFP-Nup133 and various mCherry-Nup120 variants (*D*), and full-length GFP-Nup133 carrying the R11A mutation and various mCherry-Nup120 variants (*E*).

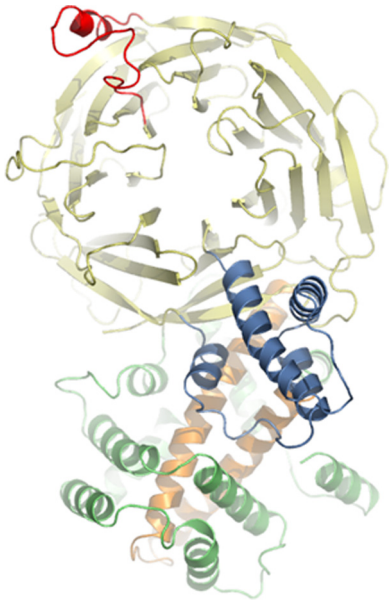

Movie S1. Rotating structure of Nup120 in ribbon representation.

Movie S1 (MOV)

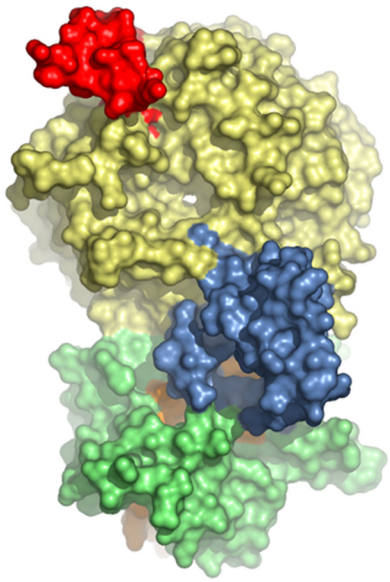

Movie S2. Rotating structure of Nup120 in surface representation.

Movie S2 (MOV)

Table S1. Crystallographic analysis

	Crystal 1	Crystal 2	Crystal 2	Crystal 3	Crystal 4
	EMTS*	Native	Native	SeMet	EMTS*
Data collection					
Synchrotron	NSLS†	APS‡	NSLS†	NSLS†	NSLS†
Beamline	X29A	GM/CA-CAT 23ID-B	X29A	X29A	X29A
Protein	Nup120 S207C	Nup120	Nup120	Nup120	Nup120
Space group	P1	P1	$P2_12_12$	$P2_12_12$	$P2_12_12$
Cell dimensions					
a, *b*, *c* (Å)	$a = 52.7$, $b = 117.5$, $c = 146.3$	$a = 53.0$, $b = 115.7$, $c = 156.1$	$a = 115.7$, $b = 156.4$, $c = 52.7$	$a = 115.1$, $b = 156.0$, $c = 52.7$	$a = 115.9$, $b = 156.8$, $c = 52.6$
α, β, γ (°)	$\alpha = 89.9$, $\beta = 89.8$, $\gamma = 89.9$	$\alpha = 90.1$, $\beta = 90.0$, $\gamma = 90.0$	$\alpha = \beta = \gamma = 90$	$\alpha = \beta = \gamma = 90$	$\alpha = \beta = \gamma = 90$
	Hg Peak			Se Peak	Hg Peak
Wavelength (Å)	1.0049	0.9795	1.0809	0.9791	1.0049
Resolution (Å)§	50.0–2.6 (2.69–2.60)	50.0–3.0 (3.11–3.00)	50.0–3.05 (3.13–3.05)	50.0–3.20 (3.31–3.20)	50.0–3.15 (3.26–3.15)
R_{sym}, %§	4.1 (41.7)	4.7 (47.8)	6.1 (74.5)	8.0 (73.5)	8.0 (82.6)
$<I / \sigma I>$§	16.9 (1.6)	40.3 (2.3)	20.2 (2.4)	18.4 (2.6)	22.6 (3.7)
Completeness, %§	95.8 (81.0)	90.5 (47.2)	99.7 (100.0)	99.8 (99.4)	100.0 (100.0)
Redundancy§	1.9 (1.7)	7.5 (4.8)	6.5 (6.4)	7.8 (7.2)	14.3 (14.6)
Refinement					
Resolution (Å)	20.0–2.6	50.0–3.0			
Number of reflections	190,898	74,274			
Test set	18,489 (8.6%)	3,174 (4.3%)			
R_{work}/R_{free}, %	23.2/25.4	25.5/27.4			
Number of atoms	22,876	22,992			
RMS deviations					
Bond angles (°)	1.3	1.5			
Bond lengths (Å)	0.008	0.010			
Ramachandran statistics¶					
Most favored, %	81.1	64.6			
Additionally allowed, %	17.7	31.3			
Generously allowed, %	1.2	4.1			
Disallowed, %	0.0	0.0			

*Ethylmercuric-thio-salicylic acid derivative.
†National Synchrotron Light Source, Brookhaven National Laboratory.
‡Advanced Photon Source, Argonne National Laboratory.
§The highest-resolution shell is given in parentheses.
¶As determined by Procheck.

Table S2. Mutagenesis of Nup120 and Nup133

Mutation	Surface patch	Residues	Binding partner	Residues	Relative binding*
Nup120 mutants					
Wild-type	NA	1–729	Nup120 NTD	1–520	+++
N200A	1	1–729	Nup133-NTD	1–520	+++
T359A	2	1–729	Nup133-NTD	1–520	+++
K362A	2	1–729	Nup133-NTD	1–520	+++
L363A	2	1–729	Nup133-NTD	1–520	+++
L427A	3	1–729	Nup133-NTD	1–520	+++
T519A	4	1–729	Nup133-NTD	1–520	+++
T551A	5	1–729	Nup133-NTD	1–520	+
Q561A	5	1–729	Nup133-NTD	1–520	+++
D578A	5	1–729	Nup133-NTD	1–520	++
I579A	5	1–729	Nup133-NTD	1–520	+
D641A	5	1–729	Nup133-NTD	1–520	–
I646A	5	1–729	Nup133-NTD	1–520	++
F647A	5	1–729	Nup133-NTD	1–520	++
T551A, I579A	5	1–729	Nup133-NTD	1–520	–
D641R	5	1–729	Nup133-NTD	1–520	–
D641R	5	1–729	Nup133-NTD R11D	1–520	–
Mutation	Region	Residues	Binding partner	Residues	Relative binding*
Nup133 mutants					
Wild-type	NA	1–520	Nup120	1–729	+++
Wild-type	NA	1–520	Nup120 β propeller	1–498	–
Wild-type	NTE	1–55	Nup120	1–729	+++
Wild-type	NTE	15–55	Nup120	1–729	–
Wild-type	NTE	1–15	Nup120	1–729	+++
K5A	NTE	1–520	Nup120	1–729	+++
R11A	NTE	1–520	Nup120	1–729	–
K12A	NTE	1–520	Nup120	1–729	+++
E13A	NTE	1–520	Nup120	1–729	+++
R11D	NTE	1–520	Nup120	1–729	–

*+++, binding indistinguishable from wild-type; ++, detectable effect; +, moderate effect; –, no binding.

Table S3. Expression constructs

Protein	Residues	Expression vector	Restriction sites 5′, 3′	N-/C-terminal sequence overhang
Bacterial expression constructs				
Nup120	1–729	pGEX-4T1-TEV	BamHI, NotI	GAMGS/none
Nup120 N200A	1–729	pGEX-4T1-TEV	BamHI, NotI	GAMGS/none
Nup120 S207C	1–729	pGEX-4T1-TEV	BamHI, NotI	GAMGS/none
Nup120 T359A	1–729	pGEX-4T1-TEV	BamHI, NotI	GAMGS/none
Nup120 K362A	1–729	pGEX-4T1-TEV	BamHI, NotI	GAMGS/none
Nup120 L363A	1–729	pGEX-4T1-TEV	BamHI, NotI	GAMGS/none
Nup120 L427A	1–729	pGEX-4T1-TEV	BamHI, NotI	GAMGS/none
Nup120 T519A	1–729	pGEX-4T1-TEV	BamHI, NotI	GAMGS/none
Nup120 T551A	1–729	pGEX-4T1-TEV	BamHI, NotI	GAMGS/none
Nup120 Q561A	1–729	pGEX-4T1-TEV	BamHI, NotI	GAMGS/none
Nup120 D578A	1–729	pGEX-4T1-TEV	BamHI, NotI	GAMGS/none
Nup120 I579A	1–729	pGEX-4T1-TEV	BamHI, NotI	GAMGS/none
Nup120 D641A	1–729	pGEX-4T1-TEV	BamHI, NotI	GAMGS/none
Nup120 D641R	1–729	pGEX-4T1-TEV	BamHI, NotI	GAMGS/none
Nup120 I646A	1–729	pGEX-4T1-TEV	BamHI, NotI	GAMGS/none
Nup120 F647A	1–729	pGEX-4T1-TEV	BamHI, NotI	GAMGS/none
Nup120 551,I579A	1–729	pGEX-4T1-TEV	BamHI, NotI	GAMGS/none
Nup120	1–498	pGEX-4T1-TEV	BamHI, NotI	GAMGS/none
Nup133	1–520	pGEX-4T1-TEV	BamHI, NotI	GAMGS/none
Nup133	56–520	pGEX-4T1-TEV	BamHI, NotI	GAMGS/none
Nup133	1–487	pET28a-PreS	NheI, NotI	GPHMAS/none
Nup133	1–487	pGEX-4T1-TEV	BamHI, NotI	GAMGS/none
Nup133 K5A	1–487	pET28a-PreS	NheI, NotI	GPHMAS/none
Nup133 R11A	1–487	pET28a-PreS	NheI, NotI	GPHMAS/none
Nup133 R11D	1–487	pGEX-4T1-TEV	BamHI, NotI	GAMGS/none
Nup133 K12A	1–487	pET28a-PreS	NheI, NotI	GPHMAS/none
Nup133 E13A	1–481	pGEX-4T1-TEV	BamHI, NotI	GAMGS/none
Nup133	520–1157	pET28a-PreS	NheI, NotI	GPHMAS/none
Nup133	520–1157	pET21d-PreS	XbaI, NotI	GPHMAS/none
Nup133	1–15	pGEX-6P1	BamHI, NotI	GST-PreS-GPLGS/HHHHHH
Nup133	1–55	pGEX-6P1	BamHI, NotI	GST-PreS-GPLGS/HHHHHH
Nup133	15–55	pGEX-6P1	BamHI, NotI	GST-PreS-GPLGS/HHHHHH
Protein	Residues	Shuffle vector	Promoter	Restriction sites 5′, 3′
Yeast expression contructs				
Nup120	1–1037	pRS416-GFP	Nup120	BamHI, NotI
Nup120	1–729	pRS416-GFP	Nup120	BamHI, NotI
Nup120	730–1037	pRS416-GFP	Nup120	BamHI, NotI
Nup120 D641A	1–1037	pRS416-GFP	Nup120	BamHI, NotI
Nup120 D641A	1–729	pRS416-GFP	Nup120	BamHI, NotI
Nup120	1–1037	pHY87-mCherry*	Nop1	BamHI, NotI
Nup120	1–729	pHY87-mCherry	Nop1	BamHI, NotI
Nup120	730–1037	pHY87-mCherry	Nop1	BamHI, NotI
Nup120 D641A	1–1037	pHY87-mCherry	Nop1	BamHI, NotI
Nup120 D641A	1–729	pHY87-mCherry	Nop1	BamHI, NotI
Nup133	1–1157	pRS315-GFP	Nop1	SalI, ApaI
Nup133	1–520	pRS315-GFP	Nop1	SalI, ApaI
Nup133	521–1157	pRS315-GFP	Nop1	SalI, ApaI
Nup133	56–520	pRS315-GFP	Nop1	SalI, ApaI
Nup133	56–1157	pRS315-GFP	Nop1	SalI, ApaI
Nup133 R11A	1–1157	pRS315-GFP	Nop1	SalI, ApaI
Nup133 R11A	1–520	pRS315-GFP	Nop1	SalI, ApaI

*HY87 (mCherry) is based on pRS416 (with the URA gene replaced by HIS).